



Universiteit  
Leiden  
The Netherlands

## **Magnetotransport properties of CrO<sub>2</sub> nanowires fabricated by selective area growth**

Prateek, K.; Bolhuis, M.; Ben Hamida, A.; Scholma, D.; Canesa Boj, S.; Aarts, J.

### **Citation**

Prateek, K., Bolhuis, M., Ben Hamida, A., Scholma, D., Canesa Boj, S., & Aarts, J. (2023). Magnetotransport properties of CrO<sub>2</sub> nanowires fabricated by selective area growth. *Journal Of Physics And Chemistry Of Solids*, 178. doi:10.1016/j.jpcs.2023.111350

Version: Publisher's Version

License: [Creative Commons CC BY 4.0 license](https://creativecommons.org/licenses/by/4.0/)

Downloaded from: <https://hdl.handle.net/1887/3704591>

**Note:** To cite this publication please use the final published version (if applicable).



# Magnetotransport properties of CrO<sub>2</sub> nanowires fabricated by selective area growth

Kumar Prateek<sup>a,1</sup>, Maarten Bolhuis<sup>b,1</sup>, Aymen Ben Hamida<sup>a</sup>, Douwe Scholma<sup>a</sup>,  
Sonia Conesa Boj<sup>b</sup>, Jan Aarts<sup>a,\*</sup>

<sup>a</sup> Huygens-Kamerlingh Onnes Laboratory, Leiden University, P.O. Box 9504, Leiden 2300 RA, The Netherlands

<sup>b</sup> Kavli Institute of Nanoscience, Delft University of Technology, Delft 2628 CJ, The Netherlands

## ARTICLE INFO

### Keywords:

CrO<sub>2</sub>  
Nanowires  
Halfmetallic ferromagnet  
Selective area growth

## ABSTRACT

Chromium dioxide (CrO<sub>2</sub>) nanowires with their half-metallic ferromagnetic properties have shown great promise in spintronics applications. However, growth of such wires remains challenging. We used the Selective Area growth method to fabricate high quality epitaxial CrO<sub>2</sub> wires on a TiO<sub>2</sub> substrate, using trenches oriented both along the substrate [001] *c*-axis and along the [010] *b*-axis, which are the magnetically easy and hard axis of the wire, respectively. We investigated the morphology of the wires by high-resolution transmission electron microscopy (TEM) and measured their physical properties, in particular magnetoresistance (MR) and the Anomalous Hall Effect (AHE). TEM images showed that the morphology of the wires grown along the two axes are very different. MR data show very sharp switching for *c*-axis grown wires (the easy axis), even for quite large wire widths. The AHE is found to be different for *c*-axis wires and *b*-axis wires, which we argue to be due to a different wire morphology on the nanoscale.

## 1. Introduction

Binary oxides with the rutile structure are currently of interest again, especially the ones which show good metallic conductivity. In the area of spintronics, in particular CrO<sub>2</sub>, RuO<sub>2</sub> and IrO<sub>2</sub>, plus substituted alloys have been studied in recent years. CrO<sub>2</sub> is a half-metallic ferromagnet (HFM) [1], and therefore fully spin-polarized; RuO<sub>2</sub> was recently found to be a weak collinear antiferromagnet [2] and is a prime candidate for showing the Crystal Hall effect [3]; and IrO<sub>2</sub> has been studied for its use as spin current detector [4]. The HFM nature of CrO<sub>2</sub> makes it particularly interesting for spintronics applications, with recent studies reporting on the expected performance in magnetic tunnel junctions [5], on the resistance of single domain walls [6], on Gilbert damping in epitaxial films [7], and on spin-curvature induced resistivity [8]. A significant drawback is that the compound is metastable at ambient conditions [9]. Single crystals can be synthesized using high pressure, but thin films cannot be grown with the standard physical deposition methods such as molecular beam epitaxy, sputtering, or pulsed laser deposition. Instead, a chemical vapor deposition (CVD) method has to be used, in which a precursor gas, mixed with oxygen, is led over a heated substrate. At the right substrate temperature, dissociation takes place, and CrO<sub>2</sub> is formed [10,11].

Because of relatively good lattice matching, the substrate of choice for the deposition is TiO<sub>2</sub>, and, to a lesser degree, Al<sub>2</sub>O<sub>3</sub>. Magnetotransport properties of thin films grown by the CVD method grown on either substrate have been extensively investigated [12–15]. One salient finding for films grown on TiO<sub>2</sub> is that the easy and hard axes for the magnetization lie along different directions in the crystal (easy axis is the [001] *c*-axis) than in thin and inevitably slightly strained films (easy axis often is the [010] *b*-axis). It was even observed that, through strain release, this can lead to a change of the easy (hard) axis direction, both as function of temperature and film thickness [13,16]. Observations of biaxial anisotropy can also be explained through this relaxation mechanism [16–18].

Much of this work has been done on films, but for incorporating CrO<sub>2</sub> in mesoscopic structures, the grainy nature of the films is a serious impediment. Substrate treatment plays a role in the grain morphology [16,19], and influence of grain boundaries was observed in the form of Intergrain Tunneling Magnetoresistance (ITMR) [14,15]. Grain boundaries can be avoided, however, by using the technique of Selective Area (SA) growth, which allow to grow high-quality nanowires and other structures. The technique is based on the fact that, at the required deposition conditions, CrO<sub>2</sub> grows epitaxially on TiO<sub>2</sub>, but does not form any deposit on silicon oxide (SiO<sub>x</sub>) [20]. By etching a trench in

\* Corresponding author.

E-mail address: [aarts@physics.leidenuniv.nl](mailto:aarts@physics.leidenuniv.nl) (J. Aarts).

<sup>1</sup> Equally contributing.

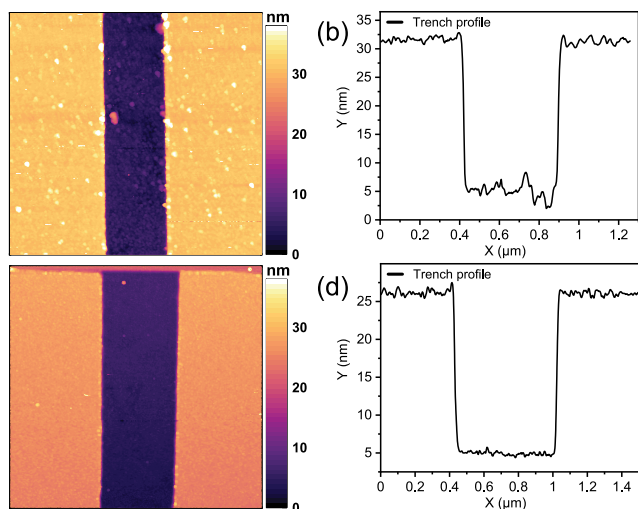


**Fig. 1.** AFM images of etched  $\text{SiO}_x$  masks on top of  $\text{TiO}_2$  substrates. The thickness of the  $\text{SiO}_x$  layer in this case is 19 nm. (a) Surface scan of a section of a mask with the trench, taken from an overetched trench (depth 26 nm). (b) The corresponding line profile of the trench showing a rough and damaged  $\text{TiO}_2$  surface at the bottom. (c) Surface scan of an optimally etched trench (depth 21 nm). (d) The corresponding line profile showing a smooth surface at the bottom.

a  $\text{SiO}_x$  layer deposited on the  $\text{TiO}_2$  substrate, high quality nanowires can be grown. The magnetotransport properties of such wires were studied [21–24] and more recently, they were used to investigate spin-triplet superconductivity [25] and the resistance of a single domain wall (DW) [26], which is of particular interest in half metals.

Given the fact that  $\text{CrO}_2$  nanowires are of clear interest for a variety of spintronics phenomena as referred to above, little attention has been paid to the growth and the morphology. It was reported that lateral overgrowth occurs when the growing layer reaches the top of the  $\text{SiO}_x$  mask, and is accompanied by the formation of side facets [20,25], but also that the initial growth can be quite defective, with a high dislocation density [20], or even voids [25].

In this paper, we make a detailed study of the morphology of SA-grown nanowires, and combine this with magnetotransport experiments. We focus on growing wires on  $\text{TiO}_2(100)$ , with directions along the substrate  $c$ -axis and  $b$ -axis (the magnetic easy and hard axis, respectively) for trench and wire widths in the range of 0.5  $\mu\text{m}$  to 2  $\mu\text{m}$ . We use atomic force microscopy (AFM), but more importantly Transmission Electron Microscopy (TEM) to study the morphology. The main and new finding of the study is that the wires along the two axes differ in important details, both with respect to the morphology and with respect to the magnetotransport. Most surprising, possibly, is that the Anomalous Hall Effect (AHE) is different for the two types of wires. This is very different from what is found when bars are etched in films by Ar-ion etching along the magnetic easy and hard directions [14,15], which can be understood from the difference in fabrication.

The paper is structured as follows. First we give a detailed description of the nanofabrication process which leads to SA-grown nanowires. Then we concentrate on wire widths around 0.5  $\mu\text{m}$  and give TEM and electrical and magneto-transport results for the  $c$ -axis (magnetic easy axis) wires, followed by the results for the  $b$ -axis (magnetic hard axis) wires. Because of in particular the AHE results, we finally present data on larger hard-axis wire widths, up to 2  $\mu\text{m}$ .

## 2. Selective area growth of $\text{CrO}_2$ nanowires

$\text{CrO}_2$  and  $\text{TiO}_2$  both crystallize in the rutile structure, with a tetragonal unit cell. Both structures are shown in the supplementary information (SI), section I. We use (100) oriented  $\text{TiO}_2$  substrates, which

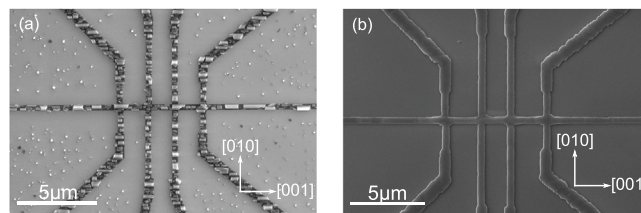


**Fig. 2.** SEM images comparing (a) growth in an overetched and rough trench bottom and (b) the growth in a smooth trench. The horizontal direction [001] in the images is the crystal  $c$ -axis, which is also the orientation of the long axis of the crystallites in (a).

means that the  $b$ - and  $c$ -axes of the structure lie in the film plane. For  $\text{CrO}_2$ , the lattice parameters are  $a = b = 0.4421$  nm and  $c = 0.2916$  nm. For  $\text{TiO}_2$  the values are  $a = b = 0.4594$  nm,  $c = 0.2958$  nm. The  $\text{CrO}_2$  values in the plane are therefore smaller by  $-3.8\%$  ( $b$ -axis) and  $-1.5\%$  ( $c$ -axis), resulting in tensile strain. In  $\text{CrO}_2$  films on HF-treated substrates, comparatively lower strain along  $c$ -axis leads to crystallites oriented along the  $c$ -direction [16]. As was already mentioned, the crystallographic  $c$ -axis is the magnetic easy axis, while the  $b$ -axis is the hard axis. Hereafter, we call  $c$ -axis oriented wires as ‘easy’ wires and  $b$ -axis oriented wires as ‘hard’ wires.

Making the  $\text{SiO}_x$  mask starts with a HF etch of the  $\text{TiO}_2$  substrate, depositing a  $\text{SiO}_x$  layer with a typical thickness of about 20–25 nm, and electron beam patterning to create a positive resist mask with the desired device structure. The trench is selectively etched into the  $\text{SiO}_x$  by reactive ion etching. After that,  $\text{CrO}_2$  nanowires are grown in the trenches using CVD in a two-zone furnace, where the substrate temperature is kept at 390  $^\circ\text{C}$ , while the precursor  $\text{CrO}_3$  is heated to 260  $^\circ\text{C}$  in the presence of a flow of  $\text{O}_2$  carrier gas. The temperature window for growth is very narrow, not more than 10  $^\circ\text{C}$ . We found that, for successful growth, it is critical to neither underetch nor overetch the trench. The result of underetching is clear, the trench bottom will then still be formed by  $\text{SiO}_x$ , and  $\text{CrO}_2$  cannot grow. Overetching is also detrimental, however, as it damages the underlying  $\text{TiO}_2$  surface. Fig. 1 compares the AFM images of two trenches, an overetched one with a depth of about 26 nm, and an optimally etched one of 21 nm. Fig. 1(a) has a rough bottom while Fig. 1(c) is very smooth, and that translates into the growth. Fig. 2(a) shows SEM images of wire growth on a rough trench surface. This causes formation of unevenly distributed  $\text{CrO}_2$  crystallites that fail to merge timely, resulting in a broken wire growth. However, for an optimally etched smooth trench as seen in Fig. 2(b), the crystallites merge completely at the bottom surface of the trench and we get high quality epitaxial growth. The depth window where we get desired trench quality to facilitate good nanowire growth is rather small, not more than a few nm. That means not only the etching, but also the  $\text{SiO}_x$  deposition has to be monitored carefully, while also the uniformity of the deposition is important. In our optimized procedure we deposit on both a ‘device’ substrate and a ‘test’ substrate in the same run. On the test substrate we measure the actual  $\text{SiO}_x$  thickness by small-angle X-ray diffraction, an etch run is performed, and AFM is used to measure the resulting trench depth. From AFM images the etch rate is computed and used in growing the wire on the ‘device’ substrate. Afterwards, devices are inspected by SEM. We grew  $\text{CrO}_2$  nanowires along different angles with respect to the  $\text{TiO}_2$  substrate axes. Here, we will focus on the easy [001] and hard [010] wires while intermediate angles are discussed in the SI, section III [27].

As a side note,  $\text{CrO}_2$  nanowires have also been SA-grown in considerably deeper trenches, of about 100 nm [24,26]. We have not investigated growth in such deeper trenches.

## 3. Resistivity as function of temperature: easy and hard wires

The temperature dependence of the resistivity,  $\rho(T)$ , is an important characterization parameter. The transport measurements were carried

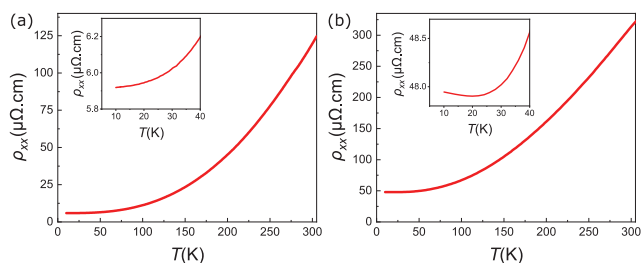


**Fig. 3.** Resistivity as a function of temperature for (a) an easy wire (width 580 nm, thickness 105 nm, contact distance 4  $\mu\text{m}$ ); the inset shows the positive temperature coefficient of resistance at lower temperature. (b) a hard wire (width 610 nm, thickness 60 nm, contact distance 2.5  $\mu\text{m}$ ); the inset shows an upturn in resistance below 20 K.

out over a temperature range from 300 K to 10 K in a Physical Property Measurement System (PPMS). Fig. 3(a) shows  $\rho(T)$  for a typical easy wire: a width around 580 nm, a thickness of 105 nm and with a distance between the contacts around 4  $\mu\text{m}$ . The room temperature resistivity  $\rho_{300}$  is 120  $\mu\Omega\text{ cm}$  while the low-temperature (10 K) value  $\rho_0$  is 5.9  $\mu\Omega\text{ cm}$ . This gives a residual-resistance ratio (RRR, the ratio between  $\rho_{300}$  and  $\rho_0$ ) of  $\approx 21$ . The wire has a positive temperature coefficient of resistance at all temperatures, also at the lowest temperatures, as seen in the inset of Fig. 3(a). This suggests very little or no grain boundary scattering of electrons [24]. We also notice that in our easy wire, while  $\rho_0$  is similar,  $\rho_{300}$  is more than 2 times lower compared to previous studies on films and SA-grown nanowires [12,15,24], indicating higher conductivity (or better metallic behavior) of our nanowires at room temperature. This suggests better crystal quality of the wires, which is supported by TEM analysis on an easy wire that is discussed in the next section.

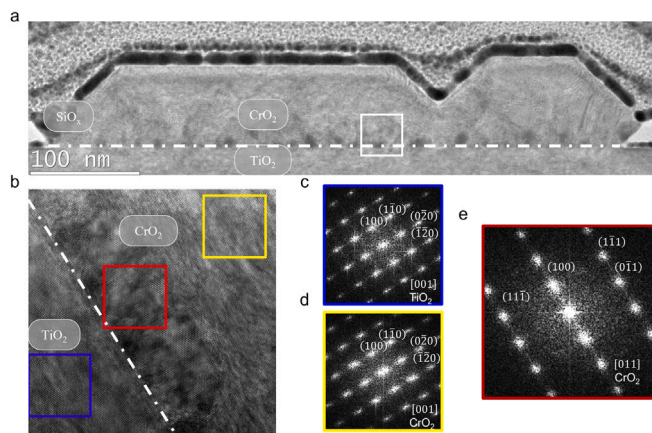
As mentioned in Section 2, we observe that for both easy and hard wires, the preferred direction of crystallite growth is the  $c$ -axis, i.e. along the easy wire length, but along the hard wire width. This makes growing hard wires more difficult. They are more sensitive to the trench depth, and also the width cannot be too small. We found the minimal width for reproducible good growth to be about 500 nm, unlike easy wires which we could grow down to a width of  $\approx 100$  nm.

Fig. 3(b) shows  $\rho(T)$  for a similar but hard wire: a width around 610 nm, a thickness of 60 nm, and distance between the contacts of 2.5  $\mu\text{m}$ . For this wire,  $\rho_{300}$  is 314  $\mu\Omega\text{ cm}$  while  $\rho_0$  is 47  $\mu\Omega\text{ cm}$ , yielding an RRR of 6.7. These numbers are similar to the epitaxial hard wires measured in Ref. [24] but significantly higher than Ar ion-etched wires from thin films [15]. Since the growth kinetics for a SA-grown hard wire is totally different from the hard wire obtained from a  $\text{CrO}_2$  film through Ar ion-etching, it is not reasonable to compare the  $\rho(T)$  measurements. We further observe that there is a small upturn in  $\rho$  at low temperature around 20 K, as seen in inset of Fig. 3(b). This indicates the presence of grain boundaries in the nanowire, that become more dominant at lower temperatures [24]. The morphology of the hard wire is further explained in details in Section 5.1.

## 4. Easy axis wires

### 4.1. TEM analysis

Using high-resolution transmission electron microscopy (HR-TEM), we analyzed the crystal structure and orientation of the nanowires and compared them to the single crystal  $\text{TiO}_2$  substrate. A low magnification image of a cross-section of the easy nanowire is given in Fig. 4(a) wherein, we can see the  $\text{TiO}_2$  substrate at the bottom with the  $\text{CrO}_2$  nanowire on top of  $\text{TiO}_2$ . The nanowire grew inside the 517 nm wide trench that was etched in the  $\text{SiO}_x$  mask (shown in white in Fig. 4(a)) that was deposited on the  $\text{TiO}_2$  substrate. The cross-section also clearly shows no  $\text{CrO}_2$  growth on top of the  $\text{SiO}_x$  mask. Contrary



**Fig. 4.** TEM inspection of a cross-section from the  $\text{CrO}_2$  nanowire along the easy axis. (a) Low resolution TEM image of the  $\text{TiO}_2$  substrate at the bottom and the partially grown  $\text{CrO}_2$  nanowire in between the  $\text{SiO}_x$  mask. (b) High-resolution TEM image of the dark cluster highlighted in (a) showing the  $\text{TiO}_2$  substrate at the bottom (blue box) and two  $\text{CrO}_2$  crystal domains with different crystal orientations (red and yellow boxes). (c–e) The indexed fast Fourier transforms of the areas highlighted in (b) (blue box in (c), yellow box in (d), red box in (e)). The FFT's show that most of the nanowire grows epitaxially with the substrate, but some crystal domains have a different orientation than the substrate.

to previous report by Singh et al. [25] we observe no overgrowth for the easy wire. However, we still observe the formation of side facets. These facets are oriented at a  $90^\circ$  angle with respect to the edge of the  $\text{SiO}_x$  mask and a  $45^\circ$  angle with respect to the  $\text{TiO}_2$  substrate, as seen near the bottom right in Fig. 4(a). The nanowire is 75 nm high and 525 nm wide at its highest and widest point, respectively. The trapezoidal shape of the wire is only interrupted by a triangular divot. A higher resolution image of the area underneath the divot is shown in the SI, Fig. S2a of the SI [27]. The area underneath the divot, right at the interface between the  $\text{TiO}_2$  substrate and the  $\text{CrO}_2$  nanowire, has several regions with a darker contrast. An HR-TEM image of one of these regions, highlighted by the white box in Fig. 4(a), is shown in Fig. 4(b). This atomic resolution image shows the  $\text{TiO}_2$  substrate in the bottom left corner and two different crystal  $\text{CrO}_2$  domains on the right. The fast Fourier transform (FFT) of the area in the blue box helps us to establish that the  $\text{TiO}_2$  crystal substrate is oriented along the [001] zone-axis as expected for the easy nanowire. As mentioned before in Section 2, we would expect the  $\text{CrO}_2$  nanowire to grow epitaxially because of the minor lattice mismatch between the  $\text{TiO}_2$  and the  $\text{CrO}_2$ . However, we observe two different  $\text{CrO}_2$  crystal orientations in Fig. 4(c). Indeed, the FFT of the area inside the yellow box, just like the bulk of the nanowire, corresponds to the diffraction pattern of  $\text{CrO}_2$  orientated along the [001] zone axis. However, the FFT of the area in the red box corresponds to the diffraction pattern of  $\text{CrO}_2$  orientated along the [011] zone axis. This shows that the bulk of the  $\text{CrO}_2$  grows epitaxially on the  $\text{TiO}_2$  substrate, but some small regions have a different crystal orientation than the  $\text{TiO}_2$  substrate. An atomic model of the different crystal domains is displayed in Fig. S2b of the SI [27]. These irregularities in the crystal orientation can mostly be found at the interface between the  $\text{TiO}_2$  substrate and the  $\text{CrO}_2$  nanowire or at the interface with the  $\text{SiO}_x$  mask. This is probably due to imperfections in the  $\text{TiO}_2$  substrate caused by the over-etching of the  $\text{SiO}_x$  mask or conversely by leaving a  $\text{SiO}_x$  residue by under-etching the  $\text{SiO}_x$  mask.

### 4.2. Magnetotransport

We further characterized  $\text{CrO}_2$  wires through magnetotransport measurements for different magnetic field orientations and at different temperatures. Fig. 5(a) shows the longitudinal magnetoresistance (MR) behavior  $(R(H_a) - R(0))/R(0) = \Delta(R)/R(0)$  at 10 K, where  $H_a$  is the

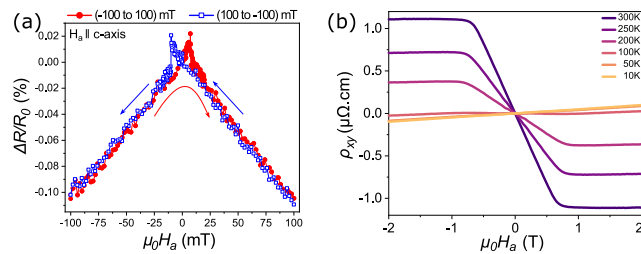


**Fig. 5.** Magnetotransport measurements on the same 580 nm wide easy wire as shown in Fig. 3. (a) In-plane longitudinal MR measured at 10 K. The external magnetic field  $H_a$  is parallel to the easy wire i.e. ( $H_a \parallel c$ -axis [001]). The field is swept from  $-100$  mT to  $100$  mT (filled red circles) and then from  $100$  mT to  $-100$  mT (open blue squares). The arrows in blue and red show the sweep direction for the respective curves. (b) Hall resistivity as a function of external out-of-plane field for the same easy wire measured at various temperatures between 10 K to 300 K. A current of  $100 \mu\text{A}$  is applied in both cases.

magnetic field along the wire axis, for the same 580 nm wide easy wire as measured in Section 3. We find that the MR behavior differs from that of previous SA-grown wires of comparable or smaller width. In contrast to earlier studies that showed parabolic behavior and an extended switching range for a similar wire width, we find that the magnetization switching is sharp, with only very little supralinear behavior when approaching the coercive field  $H_c$  at around 10 mT [24]. In earlier research, even 100 nm-wide wires did not exhibit the same degree of sharp switching as this 580 nm-wide wire demonstrates. We view this as further evidence of the high crystalline quality of the wires, possibly as a consequence of using quite shallow trenches with very well controlled bottom surfaces.

Fig. 5(b) shows measurements of the Hall resistivity as a function of external out-of-plane (OP) field for different temperatures in a range from 300 K to 10 K. The data are represented as  $\rho_{xy}$  as function of magnetic field, with  $\rho_{xy} = V_{xy}d/I$ , where  $V_{xy}$  is the transverse voltage,  $I$  is the measurement current, and  $d$  is the thickness of the wire. The behavior can, as expected, be described by

$$\rho_{xy}(H_a) = \mu_0 (R_0 H_a + R_{AHE} M) \quad (1)$$

with  $R_0$  the normal Hall coefficient,  $R_{AHE}$  the anomalous Hall coefficient, and  $M$  the magnetization of the ferromagnet. We see that  $R_{AHE}$  decreases from 300 K in a roughly linear fashion down to 100 K, where zero is reached. Below 100 K,  $R_{AHE}$  is zero. This behavior is well known, and attributed to a Berry phase, caused by an increasing amount of spin defects with increasing temperature that produce a non-trivial spin background through which the carriers move. [28,29].

The values of  $R_{AHE}$  can be compared to earlier work. According to Eq. (1),  $R_{AHE} = \rho_{xy}(0)/(\mu_0 M)$ , but the use of different units and the ambiguity with respect to the value of  $M$  (the saturation value at 300 K is lower than at 10 K, and lower than inferred from the saturation moment of  $2 \mu_B/\text{Cr-atom}$ ) make it more straightforward to compare values for  $\rho_{xy}(0)$  at 300 K. From Fig. 5(b) we find  $\rho_{xy}(0) = 1.1 \mu\Omega \text{ cm}$  for the 580 nm wide easy wire. For films measured by the van der Pauw method, values of  $1.4 \mu\Omega \text{ cm}$  [11] and  $0.8 \mu\Omega \text{ cm}$  [30] are reported. For etched films with a bar along the easy axis, two studies report  $1.5 \mu\Omega \text{ cm}$  [29,31]. No values have been reported for SA-grown wires. Interestingly, the three films yielding similar values were grown on a  $\text{TiO}_2$  substrate, while the film with a significantly lower value was grown on  $\text{Al}_2\text{O}_3$ . It is well known that such films have a different morphology, because of the hexagonal mesh of that substrate [31,32].

## 5. Hard axis wires

### 5.1. TEM analysis

We also investigated the crystal structure of the hard nanowire. The cross-section of such a wire can be seen in Fig. 6(a). Here we

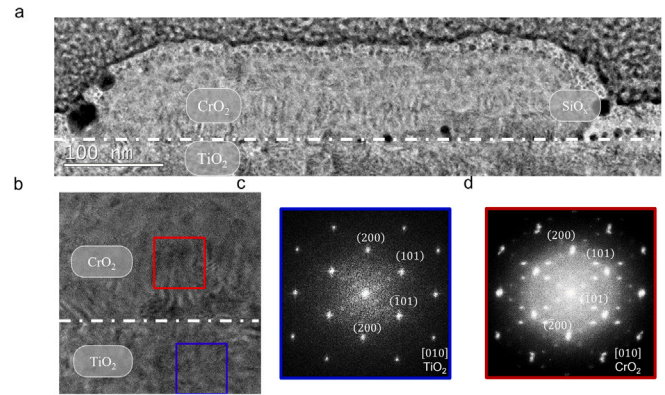


**Fig. 6.** TEM inspection of a cross-section from the  $\text{CrO}_2$  nanowire along the hard axis. (a) A low resolution TEM image of the  $\text{TiO}_2$  substrate at the bottom and the partially grown  $\text{CrO}_2$  nanowire in between the  $\text{SiO}_x$  mask. (b) A high resolution TEM image of the interface between the  $\text{TiO}_2$  substrate and the  $\text{CrO}_2$  nanowire (c) The indexed FFT of the blue box in (b). The FFT shows the hexagonal diffraction pattern of the  $\text{TiO}_2$  substrate with a [010] zone axis. (d) The indexed FFT of the red box in (b). The  $\text{CrO}_2$  FFT has the same hexagonal diffraction pattern as in (c) but has extra diffraction spots that are rotated with respect to the main hexagonal diffraction pattern. The complete indexing of all the diffraction spots in (d) is given in the SI, section V.

can see the  $\text{TiO}_2$  substrate at the bottom with the  $\text{CrO}_2$  nanowire in between the  $\text{SiO}_x$  mask. Like for the easy axis nanowire, the  $\text{CrO}_2$  grew inside the 516 nm wide trench that was etched in the  $\text{SiO}_x$  mask. The nanowire is 522 nm wide and 99 nm high at its widest and highest point, respectively. Similar to the easy wire, we observe faceted edges. Although these are less well defined than the faceted edges of the easy wire, we can still determine that the facets make roughly a  $45^\circ$  angle with the  $\text{TiO}_2$  substrate. Furthermore, the  $\text{CrO}_2$  only grows on top of the  $\text{TiO}_2$  substrate, which means that there is again no overgrowth over the  $\text{SiO}_x$  mask. An HR-TEM image of the interface between the  $\text{TiO}_2$  substrate and the  $\text{CrO}_2$  nanowire is shown in Fig. 6(b). The FFT of the region enclosed in the blue box is shown in Fig. 6(c). As expected, this pattern corresponds to the diffraction pattern of  $\text{TiO}_2$  oriented along the [0 1 0] zone axis. The FFT of the area of  $\text{CrO}_2$  inside the red box is depicted in Fig. 6(d). Here, we can see the same basic diffraction pattern corresponding to  $\text{CrO}_2$  oriented along the [0 1 0] zone axis, but more diffraction spots are visible. These Moiré patterns belong to rotated, double, and half reflections inside the crystal lattice. This indicates that the  $\text{CrO}_2$  nanowire has many crystal domains that are all rotated with respect to each other at specific angles. This Moiré pattern is present in the entire hard wire. This is different from the easy wire, where only small crystal domains along the  $\text{TiO}_2$  and  $\text{CrO}_2$  interface had a different crystal orientation. A complete indexing of all diffraction spots in Fig. 6(d) can be found in the SI, section V.

### 5.2. Magnetotransport

Fig. 7(a) shows the longitudinal MR behavior at 10 K for a hard wire (the same hard wire as measured in Section 3), with  $H_a$  the magnetic field along the wire axis, meaning  $H_a \parallel I$ , with  $I$  the applied current. Now, the results are different from both the  $2 \mu\text{m}$  etched bars [14,15] and from other SA grown hard wires of similar width [24]. Both in the etched bars and the SA grown wires, the MR showed a structure of a maximum followed by a bump, due to the several states the magnetic structure went through in the switching process. This includes an intermediate stripe-domain-like stable configuration, with the in-plane magnetization perpendicular to the wire (and therefore along the easy axis). Here, we observe a single maximum and only a small amount of hysteresis, indicating that the magnetization along the wire axis is subject to a single domain switching with only minimal additional magnetic disorder. This suggests that the shape anisotropy

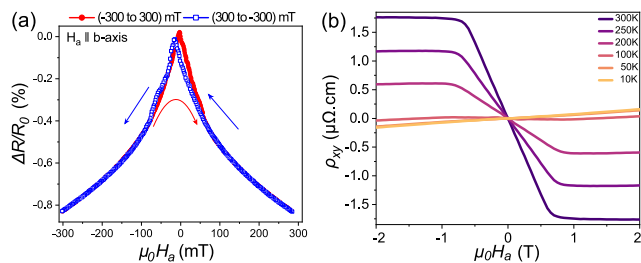


**Fig. 7.** Magnetotransport measurements on a hard wire of width 610 nm. (a) In-plane longitudinal MR plot of a hard wire measured at 10 K. The external magnetic field  $H_a$  is parallel to the hard wire axis i.e. ( $H_a \parallel b$ -axis [010]). The field is swept from  $-300$  mT to  $300$  mT (filled red circles) and then from  $300$  mT to  $-300$  mT (open blue squares). The arrows in blue and red show the sweep direction for the respective curves. (b) Hall resistivity as a function of external out-of-plane field for the same hard wire measured at various temperatures between 10 to 300 K. A 100  $\mu$ A current is applied in both cases.

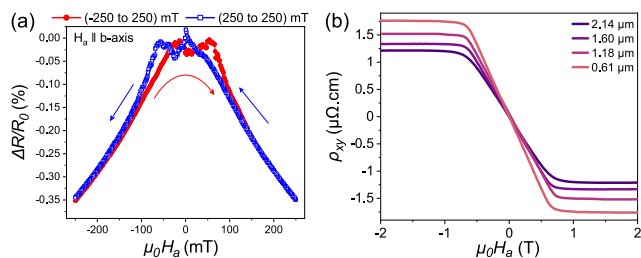


**Fig. 8.** Magnetotransport measurements on hard wires of different widths. (a) In-plane longitudinal MR plot of a hard wire of width  $1.1 \mu\text{m}$  measured at 10 K. The applied external magnetic field  $H_a$  is parallel to the hard wire axis i.e. ( $H_a \parallel b$ -axis [010]). The field is swept from  $-250$  mT to  $250$  mT (filled red circles) and then from  $250$  mT to  $-250$  mT (open blue squares). The arrows in blue and red show the sweep direction for the respective curves. (b) Comparison of Hall resistivity as a function of external out-of-plane field for the hard wires of different widths measured at 300 K shows a clear trend of  $\rho_{xy}(300)$  decreasing as the width increases.

still plays a significant role in our 610 nm wide hard wire, unlike earlier SA-grown wires where magneto-crystalline anisotropy already dominated the shape anisotropy at a width of 350 nm.

Also the Hall measurements on the hard wire differ when comparing to the previous studies. Fig. 7(b) shows  $\rho_{xy}$  for different temperatures in a range from 300 K to 10 K. The behavior again follows Eq. (1) but the values for  $\rho_{xy}(0)$  are almost 50% larger than for the easy wires of similar width. For  $\rho_{xy}(0)$  at 300 K, in particular, we find a value of  $1.75 \mu\Omega \text{ cm}$ , compared to  $1.1 \mu\Omega \text{ cm}$  for the easy wire. The significance of this result is that it shows the hard-axis material to be different from the soft-axis material, as actually seen from the HR-TEM results described in Section 5.1. For a single type of material, Onsager's principle would say that  $\rho_{xy} = -\rho_{yx}$  regardless of crystal orientation, as was indeed found for etched bars [29].

## 6. Wider hard wires

To further investigate the unexpected MR and AHE results obtained for the 610 nm hard wire, we fabricated wider hard wires, with widths of approximately  $1.10 \mu\text{m}$ ,  $1.67 \mu\text{m}$ , and  $2.26 \mu\text{m}$ . TEM images from cross-sections of these wires can be found in the SI, section IV. Although no significant morphological differences were observed between hard wires of varying widths, including the wire from Section 5.1, the transport measurements revealed a dependence on the width. Fig. 8(a) shows typical MR behavior of the  $1.10 \mu\text{m}$  wire at 10 K. Here, we see the double maximum structure which is similar to the MR behavior observed in previous studies for films and wires [14,15,24]. This suggests that at a width of around  $1 \mu\text{m}$ , the point is reached where magnetocrystalline anisotropy dominates shape anisotropy. We observe

a similar trend in the Hall data. Fig. 8(b) compares the Hall resistivity at 300 K on hard wires of different widths. As the width increases,  $\rho_{xy}(0)$  at 300 K decreases and gets closer to the value obtained for the easy wire described in Section 4.2. It is likely that for hard wires wider than  $2 \mu\text{m}$ , the behavior of the hard and easy wires becomes comparable, and that we are then essentially in the film regime. This can be understood from a growth point of view, since typical crystallites in films have dimensions of the order of a few  $\mu\text{m}$ . A trench of that width will have less confining influence on the growth.

## 7. Summary

In summary, we have shown that we can grow high quality  $\text{CrO}_2$  nanowires using the Selective Area (SA) growth on a  $\text{TiO}_2$  substrate along both the  $c$ -axis (easy axis) and the  $b$ -axis (hard axis). For the best results, a high degree of control over the etching of the trench is required. Growing hard wires is more challenging due to higher lattice mismatch between  $\text{TiO}_2$  and  $\text{CrO}_2$  along the  $b$ -axis. High-resolution TEM imaging shows that the material has a different morphology on the nanoscale, with the presence of multiple crystal domains that are rotated with respect to each other. The electrical and magnetic properties of the wires generally are in line with the picture coming from TEM.

Our wires are found to be highly conductive, in particular the easy wires, with a room temperature value for  $\rho_{300}$  of  $120 \mu\Omega \text{ cm}$  and an RRR of 21. Hard wires are less conducting, as can be expected from the TEM results. The same is true for magnetotransport properties where we find very sharp switching for quite wide easy wires, and different behavior for hard wires. Of special interest is the difference in the AHE for both wire types, which once more reflects the difference in morphology. When trenches become wider than roughly  $2 \mu\text{m}$ , the differences between (easy)  $c$ -axis wires and (hard)  $b$  axis wires disappear.

## CRedit authorship contribution statement

**Kumar Prateek:** Growth, Magnetotransport measurements, Data analysis, Writing first draft. **Maarten Bolhuis:** Transmission Electron Microscopy sample preparation, Data analysis, Writing first draft. **Ay-men Ben Hamida:** Magnetotransport measurements, Data analysis. **Douwe Scholma:** Growth, Growth and sample characterization. **Sonia Conesa Boj:** Discussions, Writing – review & editing. **Jan Aarts:** Discussions, Writing – review & editing.

## Declaration of competing interest

The authors declare the following financial interests/personal relationships which may be considered as potential competing interests: Jan Aarts, Prateek Kumar, Maarten Bolhuis, Douwe Scholma, Sonia Conesa Boj reports financial support was provided by Dutch Research Council Domain Science.

## Data availability

Data will be made available on request.

## Acknowledgments

Technical support from M. B. S. Hesselberth and Thomas Mechielsen is gratefully acknowledged. This work is part of the research program of the Netherlands Organisation for Scientific Research (NWO). The work was supported by the Intel Corporation through grant CG#38084911. The work was further supported by the EU COST action CA16218 “NanocoHybri” and by a grant from the Leiden-Delft Consortium “NanoFront”. M.B. and S.C.-B. acknowledge financial support from ERC through the Starting Grant “TESLA”, grant agreement No. 805021.

## Appendix A. TEM sample preparation and measurements

The cross-sections of the various nanowires were prepared for TEM inspection using a Focused Ion Beam (FIB) system (The Thermo Scientific™ Helios™ G4 CX DualBeam™ System). The acceleration voltage for the ion beam was set at 30 kV. Before starting the FIB process, a thin layer of gold was sputtered on top of the samples in order to prevent charring effects on the insulating TiO<sub>2</sub> substrate. During the FIB process the CrO<sub>2</sub> nanowire was protected by a platinum layer, deposited in situ using a MultiChem™ system. Tungsten was used whenever platinum was unavailable. The TEM measurements were carried out using a Thermo Scientific™ Titan 60–300 cubed TEM, operated at 300 kV. The TEM samples were oriented in a zone-axis using a double tilt holder. The HR-TEM images were recorded using a Thermo Scientific™ Ceta-16M CMOS camera.

## Appendix B. Supplementary data

Supplementary material related to this article can be found online at <https://doi.org/10.1016/j.jpccs.2023.111350>.

## References

- [1] R.J. Soulen, J.M. Byers, M.S. Osofsky, B. Nadgorny, T. Ambrose, S.F. Cheng, P.R. Broussard, C.T. Tanaka, J. Nowak, J.S. Moodera, A. Barry, J.M.D. Coey, Measuring the spin polarization of a metal with a superconducting point contact, *Science* 282 (5386) (1998) 85–88, <http://dx.doi.org/10.1126/science.282.5386.85>.
- [2] Z.H. Zhu, J. Stremper, R.R. Rao, C.A. Occhialini, Pellicciari, Y. Choi, T. Kawaguchi, H. You, J.F. Mitchell, Y. Shao-Horn, R. Comin, Anomalous antiferromagnetism in metallic RuO<sub>2</sub> determined by resonant X-ray scattering, *Phys. Rev. Lett.* 122 (2019) 017202, <http://dx.doi.org/10.1103/PhysRevLett.122.017202>.
- [3] L. Šmejkal, R. González-Hernández, T. Jungwirth, J. Sinova, Crystal time-reversal symmetry breaking and spontaneous Hall effect in collinear antiferromagnets, *Sci. Adv.* 6 (2020) eaaz8809, <http://dx.doi.org/10.1126/sciadv.aaz8809>.
- [4] K. Fujiwara, Y. Fukuma, J. Matsuno, H. Idzuchi, Y. Niimi, Y. Otani, H. Takagi, 5d Iridium oxide as a material for spin-current detection, *Nature Commun.* 4 (2013) 2893, <http://dx.doi.org/10.1038/ncomms3893>.
- [5] Z. Zhang, M. Cheng, Z. Fan, Y. Liu, D. Wang, K. Wang, R. Xiong, Z. Lu, The high magnetoresistance performance of epitaxial half-metallic CrO<sub>2</sub>-based magnetic junctions, *Phys. Chem. Chem. Phys.* 25 (2023) 1848, <http://dx.doi.org/10.1039/D2CP05015C>.
- [6] L.J. Qian, S. Zhou, K. Wanga, G. Xiao, Resistance of single domain walls in half-metallic CrO<sub>2</sub> epitaxial nanostructures, *Nanoscale* 13 (2021) 20034, <http://dx.doi.org/10.1039/D1NR05555K>.
- [7] Z. Zhang, M. Cheng, Z. Yu, Z. Zou, Y. Liu, J. Shi, Z. Lu, R. Xiong, Ultralow Gilbert damping in CrO<sub>2</sub> epitaxial films, *Phys. Rev. B* 102 (2020) 14454, <http://dx.doi.org/10.1103/PhysRevB.102.014454>.
- [8] L.J. Qian, W. Chen, G. Xiao, Spin curvature induced resistivity in epitaxial half-metallic CrO<sub>2</sub> thin films, *Nanoscale* 12 (2020) 3958, <http://dx.doi.org/10.1039/C9NR09443A>.
- [9] J.M.D. Coey, M. Venkatesan, Half-metallic ferromagnetism: Example of CrO<sub>2</sub> (invited), *J. Appl. Phys.* 91 (10) (2002) 8345, <http://dx.doi.org/10.1063/1.1447879>.
- [10] K.P. Kämper, W. Schmitt, G. Güntherodt, R.J. Gambino, R. Ruf, CrO<sub>2</sub> - a new half-metallic ferromagnet? *Phys. Rev. Lett.* 59 (1987) 2788, <http://dx.doi.org/10.1103/PhysRevLett.59.2788>.
- [11] X.W. Li, A. Gupta, T.R. McGuire, P.R. Duncombe, G. Xiao, Magnetoresistance and Hall effect of chromium dioxide epitaxial thin films, *J. Appl. Phys.* 85 (8) (1999) 5585–5587, <http://dx.doi.org/10.1063/1.369807>.
- [12] A. Gupta, X.W. Li, G. Xiao, Magnetic and transport properties of epitaxial and polycrystalline chromium dioxide thin films (invited), *J. Appl. Phys.* 87 (9) (2000) 6073–6078, <http://dx.doi.org/10.1063/1.372616>.
- [13] G. Miao, G. Xiao, A. Gupta, Variations in the magnetic anisotropy properties of epitaxial CrO<sub>2</sub> films as a function of thickness, *Phys. Rev. B* 71 (2005) 094418, <http://dx.doi.org/10.1103/PhysRevB.71.094418>.
- [14] C. König, M. Fonin, M. Laufenberg, A. Biehler, W. Bührer, M. Kläui, U. Rüdiger, G. Güntherodt, Micromagnetism and magnetotransport properties of micron-sized epitaxial CrO<sub>2</sub>(100) wires, *Phys. Rev. B* 75 (14) (2007) <http://dx.doi.org/10.1103/physrevb.75.144428>.
- [15] M.S. Anwar, J. Aarts, Anomalous transport in half-metallic ferromagnetic CrO<sub>2</sub>, *Phys. Rev. B* 88 (2013) 085123, <http://dx.doi.org/10.1103/physrevb.88.085123>.
- [16] M.S. Anwar, J. Aarts, Inducing supercurrents in thin films of ferromagnetic CrO<sub>2</sub>, *Supercond. Sci. Technol.* 24 (2011) 024016, <http://dx.doi.org/10.1088/0953-2048/24/2/024016>.
- [17] R.S. Keizer, S.T.B. Gönnerwein, T.M. Klapwijk, G. Miao, G. Xiao, A. Gupta, A spin triplet supercurrent through the half-metallic ferromagnet CrO<sub>2</sub>, *Nature* 439 (2006) 825, <http://dx.doi.org/10.1038/nature04499>.
- [18] S.T.B. Gönnerwein, R.S. Keizer, S.W. Schink, G.X. Miao, G. Xiao, A. Gupta, Planar Hall effect and magnetic anisotropy in epitaxially strained chromium dioxide thin films, *Appl. Phys. Lett.* 90 (2007) 142509, <http://dx.doi.org/10.1063/1.2715442>.
- [19] G. Miao, G. Xiao, A. Gupta, Influence of substrate treatment on the growth morphology and magnetic anisotropy of epitaxial CrO<sub>2</sub> films, *Phys. Status Solidi (A)* 203 (2006) 1513, <http://dx.doi.org/10.1002/pssa.200563108>.
- [20] A. Gupta, X.W. Li, S. Guha, G. Xiao, Selective-area and lateral overgrowth of chromium dioxide (CrO<sub>2</sub>) films by chemical vapor deposition, *Appl. Phys. Lett.* 75 (19) (1999) 2996–2998, <http://dx.doi.org/10.1063/1.125213>.
- [21] X. Zou, G. Xiao, Magnetic domain configurations of epitaxial chromium dioxide (CrO<sub>2</sub>) nanostructures, *Appl. Phys. Lett.* 91 (11) (2007) 113512, <http://dx.doi.org/10.1063/1.2784946>.
- [22] X. Zou, G. Xiao, Half-metallic chromium dioxide (CrO<sub>2</sub>) nanostructures and field-dependent magnetic domain evolution, *J. Appl. Phys.* 103 (7) (2008) 07D710, <http://dx.doi.org/10.1063/1.2832315>.
- [23] X. Zou, G. Xiao, S. Huang, T. Chen, C.-L. Chien, Magnetotransport properties of polycrystalline and epitaxial chromium dioxide nanowires, *J. Appl. Phys.* 103 (7) (2008) 07D710, <http://dx.doi.org/10.1063/1.2836800>.
- [24] X. Zou, G. Xiao, Electronic transport and magnetoresistance in polycrystalline and epitaxial CrO<sub>2</sub> nanowires, *Phys. Rev. B* 77 (5) (2008) 054417, <http://dx.doi.org/10.1103/physrevb.77.054417>.
- [25] A. Singh, C. Jansen, K. Lahabi, J. Aarts, High-quality CrO<sub>2</sub> nanowires for dissipation-less spintronics, *Phys. Rev. X* 6 (2016) 041012, <http://dx.doi.org/10.1103/physrevx.6.041012>.
- [26] W. Chen, L. Qian, G. Xiao, Resistance of domain-wall states in half-metallic CrO<sub>2</sub>, *Phys. Rev. B* 98 (2018) 174402, <http://dx.doi.org/10.1103/PhysRevB.98.174402>.
- [27] See Supplemental Material at <http://link.aps.org/supplemental/xxx> for additional details on the growth morphology of the nanowires as indicated in the main text.
- [28] J. Ye, Y.B. Kim, A.J. Millis, B.I. Shraiman, P. Majumdar, Z. Tesařovic, Berry phase theory of the anomalous Hall effect: Application to colossal magnetoresistance manganites, *Phys. Rev. Lett.* 83 (1999) 3737, <http://dx.doi.org/10.1103/PhysRevLett.83.3737>.
- [29] H. Yanagihara, M.B. Salamon, Skyrmion strings and the anomalous Hall effect in CrO<sub>2</sub>, *Phys. Rev. Lett.* 89 (2002) 187201, <http://dx.doi.org/10.1103/PhysRevLett.89.187201>.
- [30] W.R. Branford, K.A. Yates, E. Barkhoudarov, J.D. Moore, K. Morrison, F. Magnus, Y. Miyoshi, P.M. Sousa, O. Conde, A.J. Silvestre, L.F. Cohen, Coexistence of universal and topological anomalous Hall effects in metal CrO<sub>2</sub> thin films in the dirty limit, *Phys. Rev. Lett.* 102 (2009) 227201, <http://dx.doi.org/10.1103/PhysRevLett.102.227201>.
- [31] M.S. Anwar, F. Czeschka, M. Hesselberth, M. Porcu, J. Aarts, Long-range supercurrents through half-metallic ferromagnetic CrO<sub>2</sub>, *Phys. Rev. B* 82 (2010) 100501R, <http://dx.doi.org/10.1103/PhysRevB.82.100501>.
- [32] P.M. Sousa, S.A. Dias, O. Conde, A.J. Silvestre, W.R. Branford, B. Morris, K.A. Yates, L.F. Cohen, Influence of growth temperature and carrier flux on the structure and transport properties of highly oriented CrO<sub>2</sub> on Al<sub>2</sub>O<sub>3</sub>(0001), *Chem. Vapor Depos.* 13 (2007) 537, <http://dx.doi.org/10.1002/cvde.200706592>.